Potential-Induced Pitting Corrosion of a IrO_2(110)-RuO_2(110)/Ru(0001) Model Electrode Under Oxygen Evolution Reaction Conditions

Tim Weber[a,b], Johannes Pfrommer[c,d], Marcel J. S. Abb[a,b], Benjamin Herd[a,b], Omeir Khalid[a,b], Marcus Rohnke[a,b], Pirmin H. Lakner[c,d], Jonas Evertsson[e], Sergey Volkov[d], Florian Bertram[c], Raja Znaiguia[f], Francesco Carla[f], Vedran Vonk[c,d], Edvin Lundgren[e], Andreas Stierle[c,d], Herbert Over[a,b]*

a) *Physikalisch-Chemisches Institut, Justus Liebig University, Heinrich-Buff-Ring 17, 35392 Giessen, Germany*
b) *Zentrum für Materialforschung, Justus Liebig University, Heinrich-Buff-Ring 16, 35392 Giessen, Germany*
c) *Deutsches Elektronen-Synchrotron (DESY), D-22607 Hamburg, Germany*
d) *Fachbereich Physik University Hamburg, Jungiusstrasse 9, D-20355 Hamburg, Germany*
e) *Synchrotron Radiation Research, Lund University, Box 118, S-22100 Lund, Sweden*
f) *ID03 – Surface Diffraction Beamline, European Synchrotron Radiation Facility (ESRF), 71 Avenue des Martyrs, 38000 Grenoble, France*

* *Corresponding authors:* E-mail: Herbert.Over@phys.chemie.uni-giessen.de

Abstract

Sophisticated IrO_2(110)-based model electrodes are prepared by deposition of a 10 nm thick single-crystalline IrO_2(110) layer supported on a structure directing RuO_2(110)/Ru(0001) template, exposing a regular array of mesoscopic roof-like structures. With this model electrode together with the dedicated in-situ synchrotron based techniques (SXRD, XRR) and ex-situ characterization techniques (SEM, ToF-SIMS, XPS) the corrosion process of IrO_2(110) in acidic environment is studied on different length scales. Potential-induced pitting corrosion starts at 1.48 V vs. SHE and is initiated at so-called surface grain boundaries, where three rotational domains of IrO_2(110) meet. The most surprising results is, however, that even when increasing the electrode potential to 1.94 V vs. SHE still 60-70 % of the IrO_2 film stays intact down to the mesoscale and atomic scale and no uniform thinning of the IrO_2(110) layer is encountered. Neither flat IrO_2(110) terraces nor single steps or grain boundaries, where only two rotational domains meet, are attacked. Ultrathin single-crystalline IrO_2(110) layers seem to be much more stable in the anodic corrosion than hitherto expected.

Key Words: Electrocatalysis, catalytic stability, anodic corrosion, oxygen evolution reaction (OER), in-situ studies, single-crystalline IrO_2(110) model electrodes, SXRD, XRR

1. Introduction

One of the major challenges with renewable energy sources such as wind and solar is its fluctuating provision of energy. Therefore, energy storage of renewable energies in chemical bonds of molecules will play a crucial role in future energy scenarios.[1] Hydrogen production by electrochemical water splitting is the method of choice. To cope with the intermittent supply of electric energy[2,3] polymer electrolyte membrane (PEM) water electrolyzers in acidic environment need to be employed since only these devices allow for a wide partial load range and high current densities. The hydrogen evolution reaction (HER) takes place at the cathode, while the sluggish counter reaction at the anode side consists of the oxygen evolution reaction (OER) for which the most efficient electrocatalyst is RuO_2.[4,5] However, due to the limiting stability in the potential range of the OER[6,7] RuO_2 needs to be (partly) substituted by IrO_2-based oxides with reasonable activity[8] and stability[9-11], even though they still corrode.

All of the corrosion studies reported so far have been conducted on polycrystalline RuO_2- and IrO_2-based electrodes. Depending on the study, Ir dissolution of polycrystalline IrO_2 was reported to occur during the OER at electrode potentials above 1.5 V[7] or starts at potentials of 1.8 V[12] versus reversible hydrogen electrode (RHE). From steady state in chronoamperometry Hackwood et al. concluded that IrO_2 films in 0.5 M H_2SO_4 are stable up to 1.95 V vs. RHE.[13] The stability of IrO_2 depends also critically on the synthesis conditions.[14] In particular, electrochemical oxidation of Ir leads to less stable electrodes compared to thermally treated iridium oxide films.[15] The lower stability and higher activity of hydrous IrO_2 in comparison with anhydrous IrO_2 was traced to its high porosity and structural flexibility.[16] In the same line of reasoning there are reports suggesting a clear correlation of OER activity and the rate of dissolution of Ru or Ir.[17,18] Recently, Kasian et al. reported that at high anodic potentials the degradation of polycrystalline IrO_2 proceeds via the formation of gaseous IrO_3.[11] From a thermodynamic point of view (Pourbaix diagram) the electrode potential drives the dissolution as long as the oxidation state of the metal ion[19] or the lattice oxygen[18] is increased the during corrosion process.

Enhancing catalytic stability is crucial to maximize the life time cycle of future PEM electrolyzers. However, in order to improve electrode stability or identify efficient mitigation strategies on a rational base, one needs to gain microscopic insight into the dissolution process that in turn calls for the study of model electrodes with low structural complexity such as provided with single-crystalline films.[8,20,21] The microscopic insights derived from such IrO_2 films might then be partly transferred to Ir-Ru-based mixed oxides.

In this contribution, we will report in-situ catalytic stability experiments on dedicated single-crystalline IrO_2(110) model electrodes, consisting of a 10 nm thick single-crystalline IrO_2(110) layer that is supported on RuO_2(110)/Ru(0001). According to density functional theory (DFT) studies the IrO_2(110) surface is the most stable and therefore most abundant one also for industrial coatings.[22,23] Indeed, high resolution transmission electron microscopy (HRTEM) experiments of IrO_2 nanoparticles indicate that the (110) and (101) planes are pronounced.[24] With in-situ surface X-ray diffraction (SXRD), X-ray fluorescence (XRF) and X-ray reflectivity (XRR) in combination with several ex-situ characterization techniques we studied the anodic degradation of IrO_2(110)-RuO_2(110)/Ru(0001) model electrodes in acidic environment for anodic electrode potentials up to 1.94 V versus standard hydrogen electrode (SHE). The observed potential-induced pitting corrosion starts from small pits in the IrO_2(110) layer which subsequently proceeds much faster in depth owing to the missing stability of the underlying ruthenium support. Surprisingly, even at 1.94 V vs. SHE about 60-70 % of the IrO_2(110) films is still intact down to the mesoscale.

2. Experimental Section

The IrO_2(110)-RuO_2(110)/Ru(0001) model electrode was prepared in a two-step process under ultra-high vacuum conditions.[25] Firstly, the ultrathin RuO_2(110) film was grown epitaxially on a single-crystalline hat-shaped Ru(0001) disk (4.7 mm diameter, MaTecK, Jülich, Germany) at a temperature of 380°C in an oxygen atmosphere of $3 \cdot 10^{-5}$ mbar for 120 min.[26,27] This surface served as template for the subsequent growth of IrO_2 with the same rutile structure as RuO_2(110). Secondly, iridium was deposited on the fully RuO_2(110)-precovered Ru(0001) sample by physical vapor deposition (PVD), utilizing a well-outgassed electron beam evaporator (EMF 3, Omicron). Iridium was oxidized at 700 K either during deposition by a background pressure of 10^{-7} mbar of O_2 or post-oxidized by 10^{-5} mbar of O_2. For the present study we prepared a nominally 10 nm thick, completely covering IrO_2(110) layer on RuO_2(110)/Ru(0001), exhibiting arrays of 200-600 nm long "roofs" that are oriented along the three high symmetry directions of the Ru(0001) substrate and are separated by 80 nm **(**cf. **Figure 1)**. The great advantage of this mesoscopic structure is that one can easily visualize them and surface grain boundaries (intersection of three rotational domains) with scanning electron microscopy (SEM). With this sophisticated model electrode we are able to study the anodic corrosion on three length scales: well-defined surface orientation (atomic scale), step edges of the mesoscale roof structures, surface grain boundaries (cf. **Figure 1**).

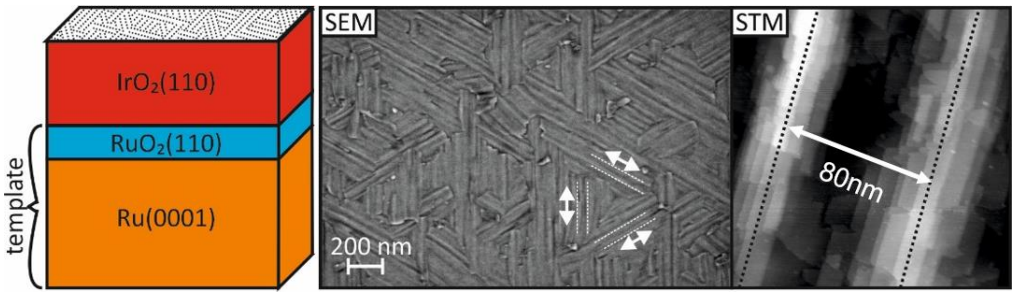

Figure 1: The freshly prepared sample with $IrO_2(110)$ layer exhibits roof-like mesostructures even visible in SEM. The oxygen-rows of $IrO_2(110)$ can be resolved with scanning tunneling microscopy (STM), indicating that the terraces of $IrO_2(110)$ are atomically well-ordered. Figure is reproduced with permission from Abb et al.[25]. © 2018 American Chemical Society.

The in-situ surface X-ray diffraction (SXRD), X-ray fluorescence (XRF), and X-ray reflectivity (XRR) experiments were carried out at beamline ID03 at ESRF, Grenoble equipped with a specifically constructed in-situ electrochemical (EC) flow cell[28,29] whose three electrodes were connected to a PAR VersaStat II potentiostat (Princeton Applied Research). The SXRD, XRF and XRR experiments used photons with an energy of 21.5 keV. With XRF we monitored in-situ the Ir-$L_{\beta1}$ emission in order to quantify the total amount of Ir in the $IrO_2(110)$ layer after subjecting the electrode to a specific anodic electrode potential. The $IrO_2(110)$-$RuO_2(110)$/Ru(0001) model electrode is housed at the bottom of the EC flow cell, while the counter electrode (CE) consists of a glassy carbon rod at the top. The reference electrode, an Ag/AgCl electrode (3.4 M KCl), is located between the working and the counter electrode. Throughout this paper the electrode potential values are given with respect to the standard hydrogen electrode (SHE) corrected for the ohmic drop due to electrolyte/cell resistance (IR drop). We used as electrolyte solution an aqueous 0.5 M H_2SO_4 solution (pH = 0.4) prepared from H_2SO_4 Suprapur® (Merck, Darmstadt, Germany) and high-purity water (18.2 MΩ·cm). The electrolyte solution was degassed by flushing with nitrogen.

First, a full set of SXRD, XRF and XRR data were taken at open-circuit potential (OCP) in H_2SO_4 (OCP = 0.89 V). Subsequently we increased the electrode potential of $IrO_2(110)$ stepwise from 1.30 V to 1.94 V by means of potentiostatic pulses with a duration of 80 s. After each potential pulse the $IrO_2(110)$-$RuO_2(110)$/Ru(0001) model electrode was set to a resting potential of 1.30 V. The main point to remind here is that the side walls of our sample, consisting of RuO_2 or metallic Ru, are unwantedly exposed to the electrolyte solution and therefore prone to readily dissolve at high anodic potentials. To overcome this unavoidable nuisance, we have to ensure with our experimental protocol that dissolved Ru complexes are not re-deposited. In doing so the electrochemical cell was purged with fresh electrolyte solution during the last 20 s of each pulse and for another 10 s at the then applied resting

potential. The SXRD, XRF and XRR data were taken in between consecutive pulses at the resting potential of 1.30 V; the data acquisition time was about 60 min. After recording the data the electrochemical cell was flushed with fresh electrolyte for 10 s. Subsequently we increased the electrode potential stepwise with the same protocol up to 1.94 V (cf. **Figure 2a**). The measured currents at the respective pulse potentials during the in-situ experiments are given in **Figure 2b**.

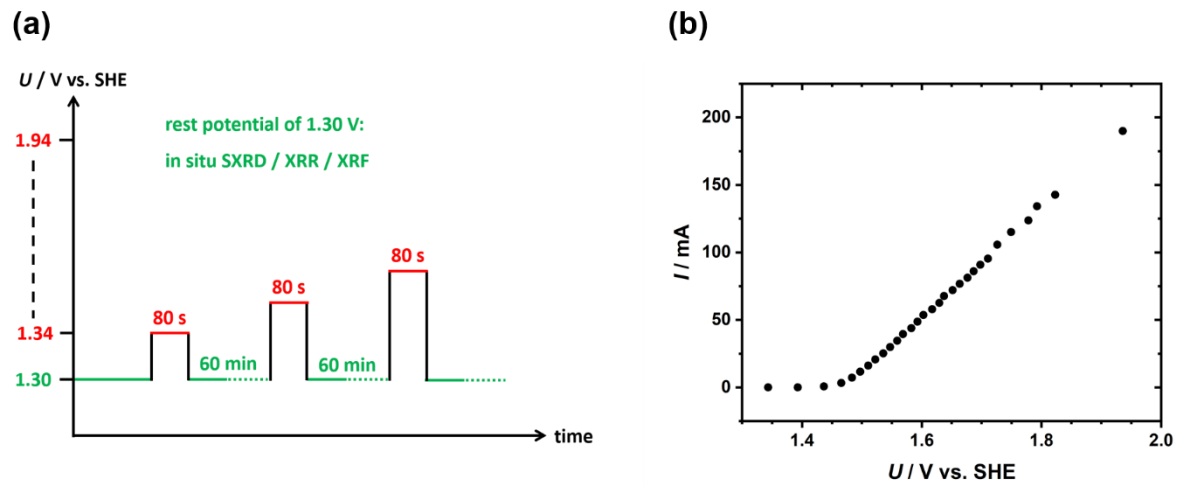

Figure 2: (a) The measurement protocol of the electrode potential variation employed in the corrosion experiments of IrO_2(110)-RuO_2(110)/Ru(0001). (b) The currents at their respective pulse potentials measured during the in situ experiments.

The in-situ experiments at the beamline were complemented with ex-situ characterization of the anodically treated IrO_2(110) films supported on RuO_2(110)/Ru(0001) after the beamtime, including X-ray photoemission spectroscopy (XPS) experiments, scanning electron microscopy (SEM), time-of-flight secondary ion mass spectrometry (ToF-SIMS), and cyclic voltammetry (CV).

The XPS experiments were conducted with the photon energy at 1253.6 eV (monochromatized Mg-K_α line) with a hemispherical analyzer (PSP Vacuum Technology). The SEM experiments were carried out with Zeiss Merlin and an acceleration voltage of 2 kV and a probe current of 100 pA. The micrographs were obtained with the secondary electron detectors (InLens or SE2).

For ToF-SIMS analysis a ToF-SIMS 5-100 (IonTOF company) was employed. The primary ion gun was operated in burst alignment mode with 25 keV Bi^+-ions as analysis species (I = 0.47 pA @ 60 µs cycle time). The 60 x 60 μm^2 probing area was scanned with 256 x 256 pixel. Depth profiling was carried out with 500 eV Cs^+ ions (I = 38.8 nA) in non-interlaced mode

and a crater size of 120 x 120 µm^2. Data evaluation was conducted with the Surface Lab 7.0 software (IonTOF company).

An additional series of ex-situ measurements (as close as possible to the potential protocol applied in the in-situ experiments) was performed to monitor alterations in the morphology and electrochemical response of the IrO_2(110) film as a function of the applied pulse potential. The pulse-rest procedure of the electrode potential was carried out in a similar EC flow cell as for the in-situ studies and comprised a potentiostatic pulse (60 s) of the desired electrode potential (starting with 1.30 V) and keeping the IrO_2(110) electrode at a resting potential of 1.30 V for 60 min. Subsequently, the sample was removed from the flow cell and placed in an electrochemical glass cell utilizing a hanging-meniscus setup so that only the IrO_2(110) surface was exposed to the electrolyte (0.5 M H_2SO_4). An Ag/AgCl electrode (sat. KCl) was used as RE, the CE consisted of a glassy carbon rod. The electrolyte solution was degassed by flushing with argon prior to the experiments while during the measurements the atmosphere above the electrolyte solution was kept in argon. The applied potentiostat was a PGSTAT302N (Autolab-Metrohm) equipped with modules enabling electrochemical impedance spectroscopy (EIS) and true analog sweeps. After electrochemical characterization of the IrO_2(110) electrode via cyclic voltammetry the sample was transferred to the SEM experiment to take SE micrographs of the electrode surface. This protocol was repeated with a stepwise increase of the pulse potential.

3. Experimental Results

Using the Ru(0001) substrate's unit cell ($a = b = 2.71$ Å, $\alpha = \beta = 90°$, $c = 4.28$ Å, $\gamma = 120°$) as reference, the *h* and *l* orientations are defined in reciprocal space. In this way, Ru-Bragg reflections appear at integer (*hkl*) values and the film reflections as non-integer (*hkl*) values which reflects the rations between the film and substrate cell parameters.[30] In **Figure 3** we summarize the SXRD data in the form of *l*- and *h*-scans for various applied electrode potentials which were corrected for the IR drop (~ 8 Ω as determined with EIS). The complete set of experimental data can be found in the Supporting Information (SI, **Figures S1-S4**). *h*-scans monitor the lateral periodicity, while *l*-scans provide information on the layer spacing and the thickness of the (110) oriented film. At open-circuit potential, the *h*-scan for $l = 1.33$ and $k = 0$ indicates clear peaks at $h = 0.73$ and $h = 1.46$ that are characteristic for a single-crystalline RuO_2(110) film grown on Ru(0001) with high degree of lateral order.[30] From this experiment we infer that IrO_2(110) adopts the same lateral lattice parameters as RuO_2(110), i.e., the IrO_2

film grow pseudomorphically on the structure-directing template RuO_2(110)/Ru(0001). Other diffraction peaks are not discernible in the *h*-scan ranging from 0.3 to 1.6.

In the corresponding *l*-scan at $h = 0.73$, $k = 0$ and OCP, a relatively broad maximum at $l = 1.29$ occurs. This peak corresponds to a layer spacing of IrO_2(110) of 3.30 Å that is significantly larger than the RuO_2(110) bulk layer spacing of 3.23 Å.[31] Using Scherrer's equation, from its full width of half maximum (FWHM) of the peak at $l = 1.29$ in the *l*-scan the thickness of the IrO_2(110) layer is estimated to be 70 Å, and from the FWHM of the peak at $h = 0.73$ in the *h*-scan a lateral domain size of 75 Å can be concluded.[30] More reliable values for the thickness of the IrO_2(110) film and its layered structure can be derived from XRR data.

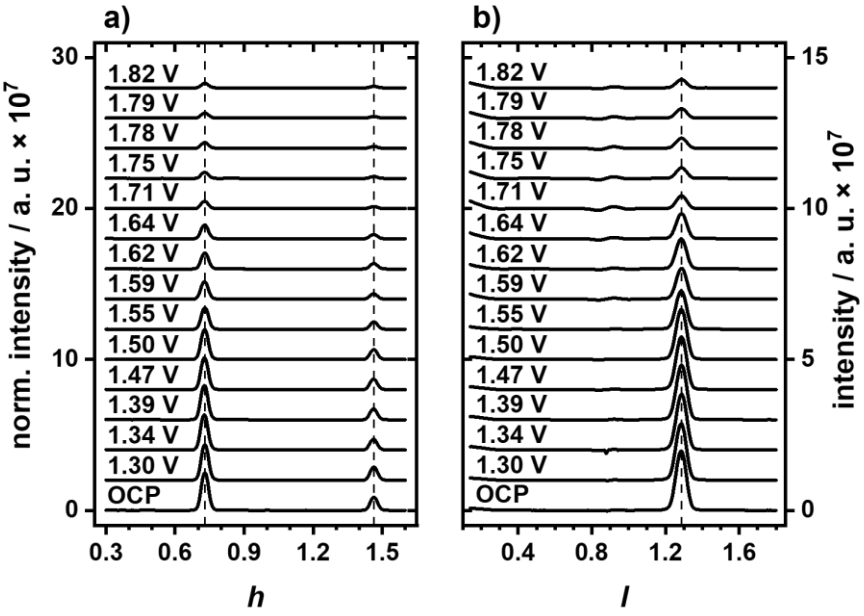

Figure 3: SXRD experiments of a nominal 10 nm thick IrO_2(110) layer grown on RuO_2(110)/Ru(0001) in the OER potential region at various electrode potentials starting from OCP up to 1.82V. a) *h*-scan at (*k*, *l*) = (0, 1.33) and b) *l*-scan at (*h*, *k*) = (0.73, 0). The dashed lines at $h = 0.73$, $h = 1.46$ and $l = 1.29$ in the *h*- and *l*-scan, respectively, indicate the peak positions of IrO_2(110). The potential-dependent scans are offset for clarity.

With increasing anodic potential the (integrated) intensity of the IrO_2(110)-related peak in the *h*- and *l*-scans decrease steadily (cf. **Figure 4**), while both the peak position and the FWHM remain constant up to an electrode potential as high as 1.82 V (cf. **Figures S5 and S6** of the SI). From these findings we infer that neither the thickness of the IrO_2(110) layer, the periodicity of the IrO_2(110) film, nor the domain size are affected by anodic polarization. The (integrated) intensity declines by 85 % when increasing the electrode potential from 1.30 V to

1.82 V. This decrease in intensity is reconciled with the removal of whole IrO_2(110) domains, while the remaining IrO_2(110) domains keep intact.

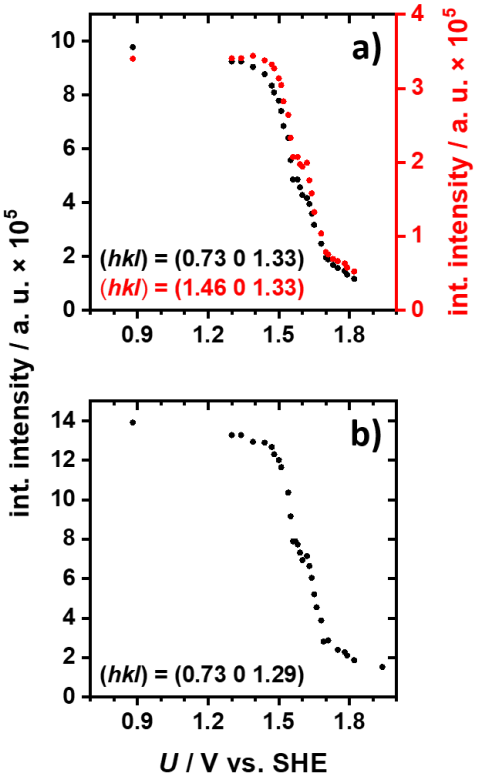

Figure 4: Integral intensity derived from the a) *h*-scan data at (*k*, *l*) = (0, 1.33) and b) *l*-scan at (*h*, *k*) = (0.73, 0) as a function of the applied electrode potential.

With in-situ XRF we quantified the Ir amount in the IrO_2(110) layer after anodic polarization to a specific electrode potential (cf. **Figure S7**). XRF probes the total amount of Ir present, unlike SXRD, which interrogates only the crystalline part of the IrO_2 film. Unfortunately, the resulting XRF data scatter quite substantially (whose reason could not be clarified) so that these data can only serve as a trend. The Ir-$L_{\beta 1}$ emission as a function of the electrode potential indicates that the Ir amount remains constant up to 1.55 V and then continuously declines. Altogether around 20 % of the Ir is lost after polarizing the IrO_2(110)-RuO_2(110)/Ru(0001) model electrode to 1.94 V. This value is substantially smaller than the derived Ir loss from SXRD, roughly 85 %, and may be indicative of a substantial disordering of the IrO_2(110) film rather than dissolution of Ir.

In **Figure 5** we present a subset of XRR data plotted against the scattering vector *q* for various electrode potentials ranging from 1.30V to 1.94 V. A summary of all recorded XRR data can be found in **Figures S8 and S9**. The solid and dashed lines indicate the positions of the maxima

and minima of the modulations in the XRR scans, respectively, that are determined by the thicknesses in the layered structure. Since these positions do not shift with increasing anodic polarization, we conclude that the geometry of the IrO_2(110)-RuO_2(100)/Ru(0001) layer is essentially unaffected by the anodic potentials up to values as high as 1.94 V. This conclusion is fully consistent with the interpretation of the SXRD data in **Figure 4**. It is important to realize that in the XRR regime merely the average electron density difference of the IrO_2(110) layer with respect to the RuO_2(110)/Ru(0001) substrate is probed, irrespective of the crystallinity.

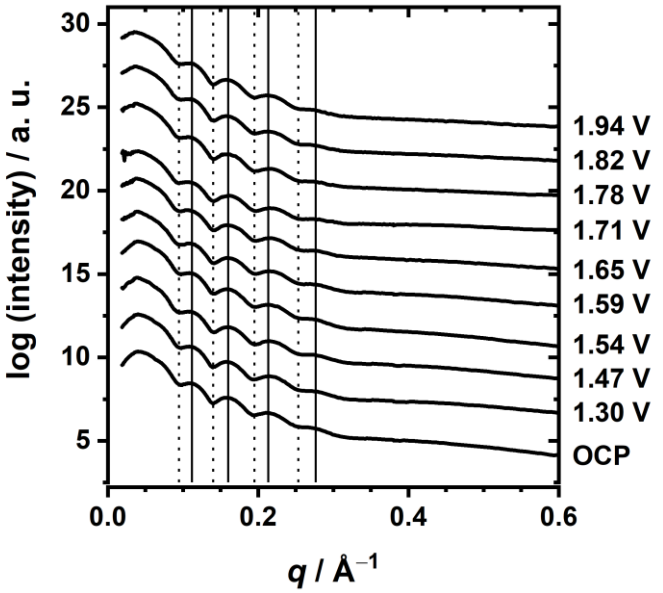

Figure 5: XRR experiments of a nominal 10 nm thick IrO_2(110) layer grown on RuO_2(110)/Ru(0001) as a function of the applied electrode potential. The solid lines indicate the positions of the maxima, the dotted lines the positions of the minima of the modulations. The potential-dependent data sets are offset for clarity.

Further analysis of the XRR data was conducted utilizing the software package GenX[32] (v 2.4.10) based on a well-founded four-layer model (for a scheme of the model see **Figure S10**). From scanning tunneling microscopy (STM) we know that the IrO_2(110) film develops roof-like structures on an otherwise flat IrO_2(110) layer. Since the IrO_2(110) film is directed by the RuO_2(110) template, three layers are well-defined, namely the IrO_2(110) roofs (roughly 2 nm high) with reduced electron density, the flat part of the IrO_2(110) layer, and the RuO_2(110) layer. As recognized for the RuO_2(110)/Ru(0001) system[29], we need to introduce a fourth layer for the RuO_2(110)/Ru(0001) interface. In **Figure S11** we compare the experimental and fitted XRR data, represented by black hollow circles and red solid lines, respectively, while the fitting parameters are summarized in **Table S1**. The most important parameters in the fitting procedure of the experimental XRR data are the thicknesses and the electron densities of the

four layers. From the fitting of the XRR data we obtain the following thicknesses of the layer: roof-like IrO_2(110) (2.17 nm), flat IrO_2(110) layer (7.90 nm), RuO_2(110) layer (1.29 nm) and RuO_2 interlayer (0.41 nm) independent of the applied electrode potential.

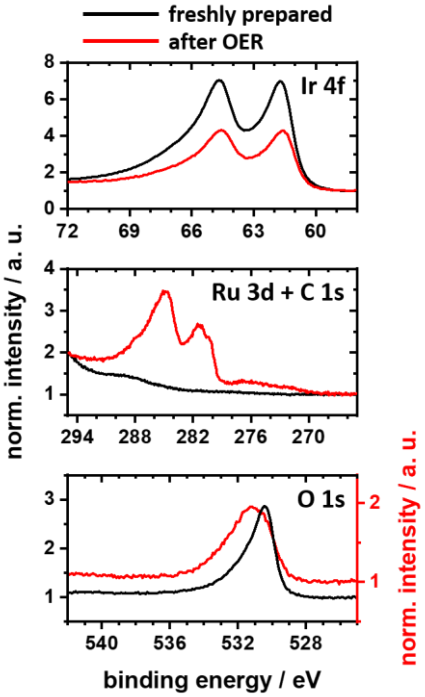

Figure 6: XP spectra of the IrO_2(110)-RuO_2(110)/Ru(0001) model electrode before and after anodic polarization up to 1.94 V. Depicted are the binding energy regions of Ir 4f (top), Ru 3d plus C 1s (middle) and O 1s (bottom).

The so-far discussed in-situ experiments were supplemented by ex-situ characterization before and after polarizing the IrO_2(110)-RuO_2(110)/Ru(0001) model electrode to 1.94 V (after the beamtime), employing XPS, SEM, and ToF-SIMS. First, XPS experiments were conducted before and after the polarization to 1.94 V. From the Ir 4f spectra in **Figure 6** we can deduce that 50% of Ir is left on the surface of the model electrode. This value is lower than the XRF-derived Ir amount, but is significantly higher than that derived from SXRD. As seen with SEM (cf. **Figure 7**) a substantial part of the IrO_2(110) film is hanging down the pit walls and therefore being hardly visible in XPS since the photoelectrons emitted by the inclined film might not be able to leave the pit efficiently. Therefore, the Ir amount derived from XPS should actually be higher than 50 %; inspection of several SEM images provides a rough estimation for the total amount of Ir of 60-70 %. Actually, the XRF data scatter quite substantially with a large uncertainty in the derived Ir amount left after the corrosion experiment: 80 ± 10%. In conclusion, the remaining Ir amount at the electrode surface after the corrosion experiment is estimated to be about 70%.

The XPS characterization of the freshly prepared model electrode exhibits no Ru signal due to attenuation by the large IrO_2(110) layer thickness (~ 10 nm as derived from the XRR data) whereas after anodic polarization up to 1.94 V the Ru 3d signal becomes clearly visible (cf. middle panel of **Figure 6**). This observation is reconciled with the exposure of Ru or (hydrous) RuO_2 through the pits seen in SEM (cf. **Figure 7**). The intensity ratio of Ru $3d_{5/2}$/Ru $3d_{3/2}$ is not 3:2, as expected from the degeneracy of the Ru 3d electronic transitions, therefore, the peak around 285 eV consists presumably of contributions from Ru $3d_{3/2}$ at 285 eV and C 1s at 285-288 eV. The O 1s peak after polarization in the OER potential region is apparently broadened, due likely to contributions from OH and H_2O of hydrous RuO_2.

With SEM we compare the IrO_2(110)-RuO_2(110)/Ru(0001) morphology before and after anodic treatment at 1.94 V. SEM reveals clearly pitting corrosion with deep holes (cf. **Figure 7a**) and large portions of the IrO_2(110) layer hang over the pit edges into the pits. In the high-resolution SE micrograph (cf. **Figure 7b**) we can even recognize the roof-structure on the intact IrO_2(110) film. But even in regions, where corrosion of RuO_2(110)/Ru(0001) occurs below the IrO_2(110) film, we can observe that IrO_2(110) is still intact although the films are inclined into the pits and breaks partly up so that with XRR and with SXRD these parts of the IrO_2(110) film become invisible. From SEM we estimate that 60% of the IrO_2(110) film might be intact. A comparison of SE micrographs of the freshly prepared and the corroded surface with identical magnification is presented in **Figure S12**.

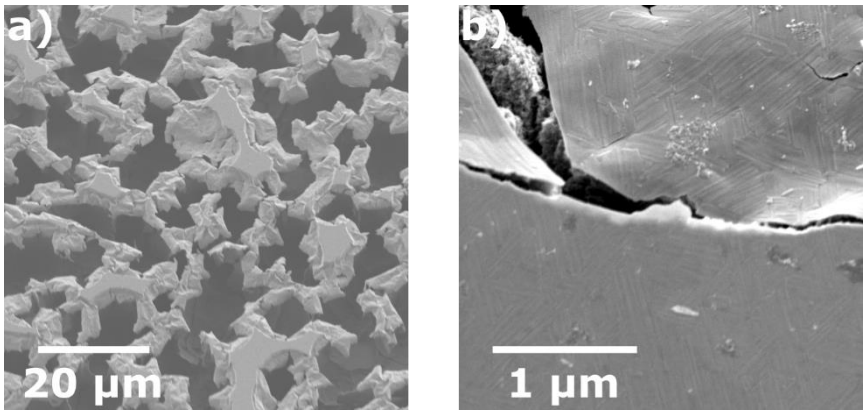

Figure 7: SE micrographs after step-wise polarization of the model electrode to 1.94 V. a) overview SE micrograph (SE2) revealing the pitting corrosion (sample tilted by 25°). b) high-resolution SE micrograph (InLens) of IrO_2(110)-RuO_2(110)/Ru(0001) model electrode. Clearly visible is the roof-like structure on part of intact IrO_2(110). If corrosion takes place below the IrO_2(110) film then the under-corroded part of the IrO_2(110) film is mechanically instable, breaks and inclines.

In **Figure 8a** the total ion image from ToF-SIMS analysis indicates clearly pitting corrosion with deep holes. From the mass-selected images (cf. **Figure 8b**) we can identify the chemical

nature of the holes and the residual films: the islands consist of IrO_2, while the holes contain only Ru/RuO_2. Since the detected RuO^- signal (cf. **Figure 8b**) originates from the crater bottom, only low intensity is detected due to shadowing effects and less focus depth of the used SIMS machine. At some of the edge regions it appears that the film hangs down the crater wall (cf. **Figure 8a)** which can be seen clearer in **Figure 8c**. Here the IrO^- mass signal, which was taken within a depth profile, is depicted in 3D representation. From the cross-sectional view the 10 nm thin $IrO_2(110)$ film can be seen, while at the edges of some of the pits the Ir-related signal reaches far below 10 nm. This confirms the impression from **Figure 8a**, that the remaining film hangs down the crater walls.

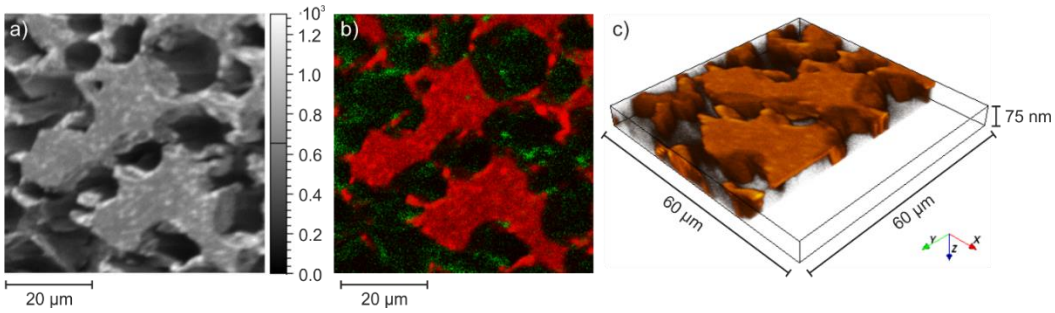

Figure 8: Spatially resolved ToF-SIMS images of the electrode after step-wise polarization to 1.94 V. a) Total ion image, which shows the surface topography b) overlay of IrO^- mass image in red and RuO^- mass image in green. The colour intensity represents the count rate of the respective mass signal. Due to the fact, that the RuO^- originates from the bottom of the crater structure, the intensity is quite low. c) 3D mapping of the IrO^- signal (side cut) of the upper electrode area. All three images show the same electrode region.

It is very likely that the Ru side walls of the sample, which might be (partly) oxidized to RuO_2 during the UHV preparation, underwent pitting corrosion as well. However, the pits after the in-situ experiments might be (at most) several tens of microns in depth whereas the single-crystalline surface is 4.7 mm in diameter. For this reason we can exclude that possible pits at the side walls affect the middle part of the single-crystalline surface from which the in-situ data are taken.

Since the previous ex-situ characterization was only performed after the $IrO_2(110)$-$RuO_2(110)/Ru(0001)$ model electrode was subjected to a potential of 1.94 V, an additional series of measurements was devised to determine the potential at which the pitting corrosion starts. Within the pulse-rest protocol the $IrO_2(110)$ surface was characterized via cyclic voltammetry and SEM for various electrode potentials. **Figure 9** shows SE micrographs of the electrode surface after applying potential pulses of a) 1.40 V and b) 1.48 V.

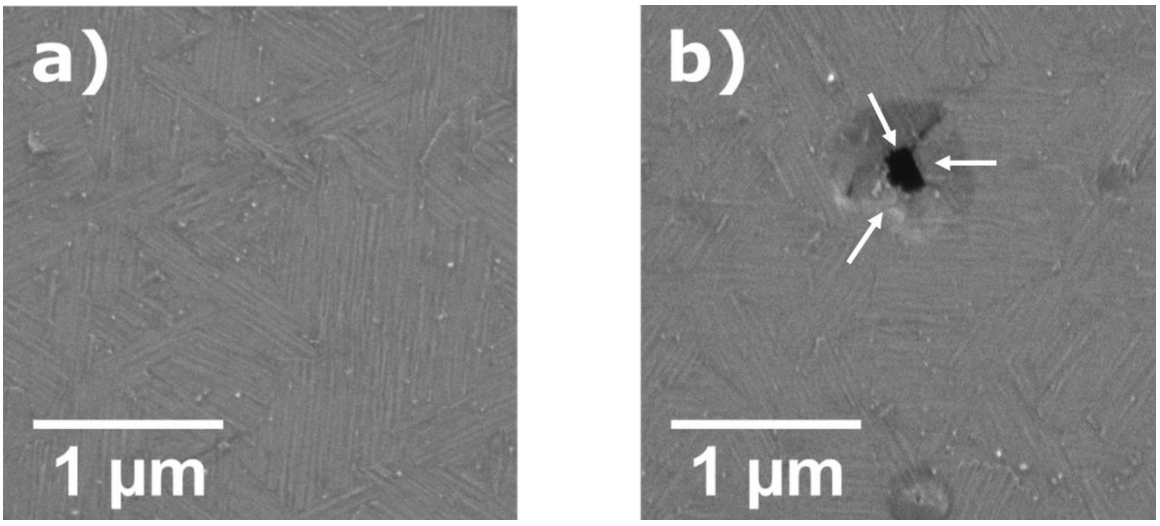

Figure 9: SE micrographs (both SE2) of the $IrO_2(110)$-$RuO_2(110)$/Ru(0001) model electrode surface after applying a potential of a) 1.4 V and b) 1.48 V. The roof-like structure of the intact $IrO_2(110)$ film is visible in both cases, whereas after the pulse to 1.48 V the first pits appear. The direction of the rotational domains around the pit are indicated by white arrows.

From **Figure 9b** it is evident that after the potential pulse to 1.48 V the first pits appear. The potential induced pit appears at the surface grain boundary where three rotational $IrO_2(110)$ domains meet. As already indicated from **Figure 7** it seems that the underlying Ru substrate is eroded, while the $IrO_2(110)$ film is still intact and hangs down the pit walls, therefore causing a ring-shaped contrast around the actually visible hole (cf. **Figure 9b**). Further SE micrographs providing an overview of the electrode surface after subjecting it to 1.40 V and 1.48 V are presented in **Figure S13**. These surface grain boundaries of the $IrO_2(110)$ film can also be studied in STM images (cf. **Figure S14**). From STM it is evident that the depressions observed in the surface grain boundaries are quite shallow (less than 1 nm deep) and therefore do not expose the underlying $RuO_2(110)$/Ru(0001) substrate.

Possible alterations in the electrochemical response of the $IrO_2(110)$ electrode surface were monitored by recording cyclic voltammograms (CVs) after the pulse-rest protocol with varying pulse potentials depicted in **Figure 10**.

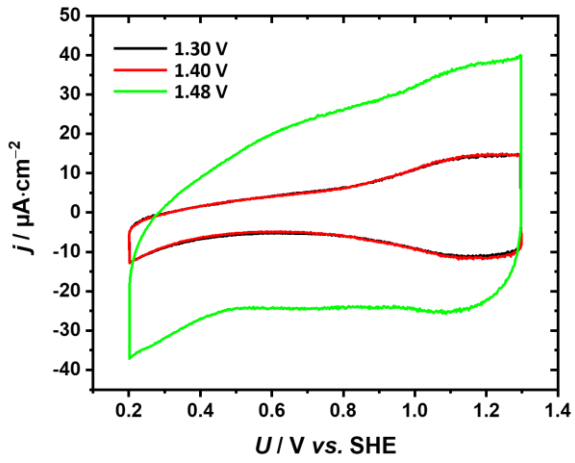

Figure 10: Cyclic voltammograms of the IrO_2(110)-RuO_2(110)/Ru(0001) model electrode after anodic polarization to the pulse potentials given in the legend. The CVs were recorded in 0.5 M H_2SO_4 utilizing a hanging-meniscus setup, the scan rate was 100 $mV \cdot s^{-1}$.

After the electrode potential pulses of 1.30 V and 1.40 V the CVs look virtually identical, with a broad feature in the potential region of 0.8 to 1.3 V that is comparable with recently published CVs of IrO_2(110) films in acidic medium[20]. After polarizing the electrode to 1.48 V the first pits appear in the SE micrograph (see **Figure 9b**) and as a result there are substantial changes in the CV. The capacitive current increases substantially from the initial IrO_2(110)-RuO_2(110)/Ru(0001) model electrode to the partly pitting corroded one. Assuming that the base of the pits are flat Ru or RuO_2 areas, the geometrical surface area would only change by a small margin; only the side walls of the pits contribute additionally to the total surface area. Therefore, from an increase of capacitive current by a factor of 3-5 we conclude that not the geometric surface area is increased but instead hydrous RuO_2, a well-known supercapacitor material[33], is formed in the pits[34]. The formation of hydrous RuO_2 is also corroborated by the O 1s XP spectrum in **Figure 6** of the initial IrO_2(110)-RuO_2(110)/Ru(0001) compared to the sample after stepwise polarization to 1.94 V. There is additional photoemission at binding energy higher than 531 eV which is indicative of water and OH groups. The potential for the initial formation of pits found by cyclic voltammetry and SEM (1.48 V) is slightly lower compared to the one at which the intensity in the XRF data starts to decrease (around 1.55 V). This difference is due likely to the fact that in the initial stage of corrosion the concentration of pits is low so that the Ir amount does practically not vary in this potential range. Since the scattering of the data is very large, XRF is not sensitive enough to monitor this small decrease in Ir amount. Hence, changes are only visible at potentials higher than 1.55 V.

4. Discussion

We designed a model electrode system that is able to provide information on the anodic corrosion of IrO_2(110) on different length scales. The roughly 10 nm thick IrO_2 layer is grown on a RuO_2(110)/Ru(0001) template with a well-defined surface orientation along the [110] direction with atomically flat (110) terraces. The rotational domains of IrO_2(110) form grain boundaries (size about 20 nm, cf. **Figure S14**) where two or three domains meet. In addition, the IrO_2(110) film exposes a periodic arrangement of roof-like structures (mesoscale: 80 nm) consisting of eight to ten ascending steps followed by the same number of descending steps separated by narrow and long (110) terraces. It is known that both RuO_2 and Ru are prone to corrode under OER conditions, while IrO_2 is significantly more resistant against anodic corrosion.[6,7,11] Therefore, the covering ultrathin IrO_2(110) film serves as a kind of protection layer for the underlying RuO_2(110)/Ru(0001) template that corrodes very fast without protection.

This model electrode is studied with dedicated in-situ and ex-situ characterization techniques addressing the corrosion behavior on these length scales depending on the applied anodic electrode potential. Each of the employed techniques "looks" differently at the corrosion process of the IrO_2(110) film. While in-situ SXRD interrogates the crystalline structure of the ordered IrO_2(110) overlayer in a specific direction (namely the [110] orientation of IrO_2 that is parallel to the [0001] direction of Ru), the in-situ XRR methods probes the layered structure (without considering crystallinity of the film) of our model electrode during anodic polarization in the OER regime. In principle the in-situ XRF would be the method of choice to monitor the kinetics of the anodic corrosion behavior of the IrO_2(110). With ex-situ XPS after anodic polarization to about 2 V, we can quantify the effect of corrosion in total quite accurately, assuming that the layer thickness of IrO_2(110) is not affected by the anodic corrosion. From SEM and also STM[25] we know that IrO_2(110) grows in three rotational domains on the RuO_2(110)/Ru(0001) template with domain boundaries where rotational domains meet (kind of oriented "surface grain boundary", cf. **Figure S14**). These surface grain boundaries can readily be imaged by ex-situ SEM due to the imposed roof-like structure on the IrO_2(110) film. Ex-situ SEM, STM and ToF-SIMS experiments after anodic corrosion are employed to visualize the effects of anodic corrosion of the IrO_2(110) model electrode from the meso- to the atomic scale. A film thickness in the order of 10 nm allows to follow corrosion phenomena directly at the electrode surface on a time scale suitable for laboratory and in-situ synchrotron based experiments, including SXRD, XRF, and XRR, since even small changes in the layer structure due to corrosion affect substantially X-ray diffraction and reflectivity. Quite in contrast, this

high sensitivity to corrosion effects is hardly achievable with a single crystal electrode of IrO_2[35], or with 15 nm thick IrO_2 polycrystalline films[7], although for these electrodes one can analyze operando the electrolyte solution for dissolved Ir-based material[7]. In addition, the ultrathin single-crystalline IrO_2(110) films used in this study exposed a roof-like mesoscopic structure that can readily be identified with SEM. Whenever we observe the roof-like structure on part of the IrO_2(110) film after a corrosion experiment we know that no (substantial) corrosion has taken place. From in-situ SXRD (*l*-scan) and XRR we learn that the thickness of IrO_2(110) film is not affected by anodic corrosion up to anodic electrode potential of 1.94 V. This means that anodic corrosion does not uniformly thin the IrO_2 film and flat terraces are stable on the atomic scale. Secondly, the roof-like mesostructure with its periodic arrangement of descending steps followed by ascending steps allows to study the role of step edges in the corrosion process. In-situ XRR and also ex-situ SEM and STM evidence that these meso-structures are not attacked by corrosion. Therefore, steps with their exposed undercoordinated Ir atoms are found to be not subject to anodic corrosion. Otherwise, the roof-like structure would shrink in size and may form top-flatted roofs due to step-induced corrosion of terraces. This is experimentally not observed in STM (cf. **Figure S15**) and SEM. Thirdly, corrosion occurs exclusively at surface grain boundaries, where three rotational IrO_2(110) domains merge. Grain boundaries with two merging domains are not subject to anodic corrosion. Ex-situ SEM experiments (cf. **Figure 9**) indicate that dissolution starts preferentially at these "surface grain boundaries" (as a typical imperfection of our single crystalline IrO_2(110) film) at 1.48 V and progressing in-depth corrosion into the Ru(0001) substrate. Regions with pitting corrosion and regions of intact IrO_2(110) coexist up to high electrode potential of 1.94 V, evidencing that perfect crystalline IrO_2(110) domains are remarkably resistant against anodic corrosion. This conclusion calls for a clear-cut experiment, where the IrO_2(110) film is supported on rutile TiO_2(110) instead of RuO_2(110)/Ru(0001). At high anodic electrode potentials we do not expect that pitting corrosion will occur for IrO_2(110)/TiO_2(110) since neither surface grain boundaries are available nor the TiO_2(110) substrate is susceptible to accelerated corrosion.

Ex-situ SEM is able to follow the initial growth of pits. Small potential-induced pits form exclusively at surface grain boundaries. From this observation we suggest that surface grain boundaries expose highly undercoordinated Ir atoms that are prone to dissolve under anodic potentials above 1.4 V vs. SHE. Once the surface grain boundary is opened and the underlying RuO_2(110)/Ru(0001) substrate is exposed to the electrolyte solution, pitting corrosion is accelerated since Ru and RuO_2 are significantly less stable than IrO_2. Corrosion is not restricted to the vertical direction, but corrosion of ruthenium leads to undercutting of the IrO_2(110) film

so that the IrO_2(110) films is slightly inclined into the pits as clearly seen in SEM (cf. **Figure 9b**) and ToF-SIMS images (cf. **Figure 8**). Upon increasing the anodic potential, O_2 bubbles will also nucleate in the pits; recall that Ru/RuO_2 is a better OER catalyst than IrO_2. These bubbles in the pits may disrupt part of the overhanging IrO_2(110) film upon releasing into the electrolyte solution, thereby leading to larger holes with straight pit walls (cf. **Figure 7**). Therefore, besides dissolution of highly undercoordinated Ir species from the surface grain boundaries, mechanical instabilities are important in the corrosion process.

It is quite surprising that each the employed in-situ techniques quantifies the degree of corrosion differently, but this shows also that each techniques has a specific look at the corrosion behavior of the film. A complete picture is evolved only when different techniques are employed. With in-situ monitoring of the SXRD intensity of IrO_2(110) related reflections in *h*-scan and *l*-scans in we found a steady degradation of crystalline part of the IrO_2(110) film with anodic potential, suggesting that after polarization to 1.94 V only 15 % of the original IrO_2(110) film is left as crystalline film in the initial orientation on the surface. From the FWHM of the of IrO_2(110) related reflections in *h*- and *l*-scans the crystalline domain size of IrO_2(110) is shown to be not affected by the polarization neither in-plane nor out-of-plane; a similar behavior of the crystalline domain size has been observed in previous UHV studies for the reduction of the RuO_2(110) layers.[30,36] In addition, the thickness of the IrO_2(110) film remains constant after anodic polarization as evidenced with in-situ XRR.

With XRF we can quantify the total amount of Ir in the IrO_2(110) film, irrespective whether Ir is in a crystalline environment or not. Unfortunately, the resulting XRF data scatter quite substantially (the reason could not be clarified) so that these data bear large uncertainties. From the XRF data we infer that only 20-30 % ± 15 % of the Ir is lost from the electrode surface after stepwise polarization to 1.94 V. This apparent contradiction of SXRD and XRF experiments can be resolved by the localized corrosion of an uniform single crystalline IrO_2(110) film as observed ex-situ by SEM (cf. **Figures 7, 9**). The pits are several µm deep due to accelerated corrosion of Ru and the formation of hydrous RuO_2 as evidenced by XPS and CV. In agreement with XRR the layer thickness of the IrO_2(110) film is not altered by localized corrosion, while the diffraction intensity in SXRD declines due to pits and IrO_2(110) flakes that are inclined into the pits with a slight mismatch of the (110) orientation from the [0001] direction of the substrate. Moreover, regions of the IrO_2 film with no pits expose the roof-like structure in SEM, indicating that these parts of the IrO_2(110) film are fully intact down to the mesoscale (SEM) and presumably down to the atomic scale (SXRD). At 1.94 V, about 60 % of the IrO_2(110) layer is intact even on the mesoscale (cf. **Figure 7b**), although surface grain boundaries are still found

on the intact IrO_2(110) part of the model electrode. Obviously, the crystallinity is decisive to the observed corrosion resistance of IrO_2(110). But maybe there is an additional process operative that facilitates corrosion resistance. With increasing anodic potentials above 1.6 V, O_2 bubbles are formed due to the oxygen evolution reaction (OER). O_2 bubbles may adhere preferentially at the edges of the pits, thereby reducing contact area of IrO_2(110) layer with the electrolyte solution and reducing the corrosion. However, O_2 adherence will not suppress corrosion since the bubbles are released. The same effect of preferential adhering of Cl_2 bubbles at the cracks was reported for the chlorine evolution reaction on dimensionally stable anodes (DSA), employing a scanning electrochemical microscope.[37]

Based on these insights gained in the present study we propose mitigations to improve stability of IrO_2-based OER catalysts. One should use core shell particles with an IrO_2 coating grown on an "inert" core such as TiO_2. The structure of TiO_2 and IrO_2 should be adapted so that rutile TiO_2 is a better choice than any other polymorph of TiO_2. In order to reduce the number of grain boundaries of IrO_2 the supporting TiO_2 nano-core should be single-crystalline. In order to improve the electronic conductivity, TiO_2 can be alloyed with 30 % RuO_2. But also the activity of the IrO_2 layer can be increased by alloying with RuO_2. Currently, mixed Ir-Ru-Ti oxides are in industrial use.[4] Here the selective corrosion of Ru may lead to porous structures in the coating with the consequence of mechanical instabilities due to abrupt O_2 bubble release.

Within the experiments presented here, the (change in) electrocatalytic activity of the IrO_2(110) film cannot be determined unambiguously. During the in-situ experiments in the EC flow cell there is always a contribution from the (oxidized) Ru side walls, which have a higher activity towards OER than IrO_2. Even when suppressing a contribution from the side walls in a hanging-meniscus setup our model electrode is not suitable for acquiring kinetic data. As soon as potential induced pitting corrosion starts there contribute at least three processes to the total current density: OER over IrO_2(110), OER over hydrous RuO_2, and oxidation/dissolution of Ru. The activity of our IrO_2(110)-RuO_2(110)/Ru(0001) model electrode will remain high even if the IrO_2(110) film is completely lost, since the RuO_2(110)/Ru(0001) support is highly active towards OER (but also highly unstable).

5. Conclusions

Although long-term stability of (electro)catalysts is of major concern in industrial catalysis, fundamental studies on stability are just emerging.[38] Sophisticated IrO_2(110)-based model electrodes are prepared by deposition of a 10 nm thick single-crystalline IrO_2(110) layer supported on a structure directing RuO_2(110)/Ru(0001) template, exposing a regular array of roof-like structures which are 2 nm high, 50-80 nm wide, and several 100 nm long. With in-

situ techniques such as surface X-ray diffraction (SXRD), X-ray fluorescence (XRF), and X-ray reflectivity (XRR) the anodic corrosion is studied on different length scales in acidic environment for electrode potentials from 1.4 V up to 1.94 V versus standard hydrogen electrode (SHE). After the in-situ corrosion experiment (polarization up to 1.94 V vs. SHE) the morphology changes are visualized by scanning electron microscopy (SEM) and time-of-flight secondary ion mass spectrometry (ToF-SIMS) and the composition was quantified by XPS. With this model electrode together with the dedicated characterization techniques the corrosion process of IrO_2(110) are studied on different length scales. The anodic corrosion process already starts at 1.48 V vs. SHE via potential-induced pitting corrosion at surface grain boundaries due to Ir dissolution (SEM). As soon as these pits reaches the RuO_2(110)/Ru(0001) interface pitting corrosion is accelerated due to the missing stability of RuO_2 and metallic Ru at high anodic potentials and leading to undercutting of the pits (SEM, ToF-SIMS). Subsequently, O_2 bubble formation in the pits causes mechanical disruption the free-standing part of IrO_2(110) layer hanging over the pits. The process of pitting corrosion is reconciled with in-situ SXRD and XRR experiments, indicating that neither the FWHM of IrO_2-related peaks in *l*- and *h*-scans varies with the corrosion potential nor the thickness of the IrO_2(110) layer is affected by the anodic electrode potential up to 1.94 V vs. SHE.

However, even at 1.94 V vs. SHE about 60-70 % of the IrO_2(110) film is still intact, exposing the original mesoscopic roof-like structures (SEM) and no uniform thinning of the IrO_2(110)layer is observed (XRR). Anodic corrosion is exclusively observed at the surface grain boundaries of the IrO_2(110) film where three rotational IrO_2 domains meet. Corrosion is not observed when only two rotational domains merge. Obviously, neither the flat terraces nor step edges of IrO_2(110) are subject to anodic corrosion (SXRD, XRR). Obviously, the degree of crystallinity of IrO_2-based electrodes is a key parameter for stability, the higher the better. On the basis of these insights, we suggest that a core-shell particle with an IrO_2-based coating on a single crystalline TiO_2 or mixed RuO_2-TiO_2 nano-core particle should improve the stability of OER anodes considerably.

Supporting Information

This material is available free of charge via the Internet at http://pubs.acs.org

- full set of *h*-scans, *l*-scans (SXRD) including plots of the peak positions and the FWHM as function of the electrode potential up to 1.94 V vs. SHE

- XRF experiments as a function of the electrode potential

- full set of XRR data for electrode potentials up to 1.94 V vs. SHE

- details of the XRR analysis including four-layer model and fitting parameters

- SE micrographs of the freshly prepared and corroded IrO_2(110)-RuO_2(110)/Ru(0001) model electrode at the same length scales

- SE micrographs of the initial corrosion of the IrO_2(110)-RuO_2(110)/Ru(0001) model electrode

- STM image of a surface grain boundary at the IrO_2(110) film supported on RuO_2(110)/Ru(0001)

- STM images of the freshly prepared and corroded IrO_2(110)-RuO_2(110)/Ru(0001) model electrode

Acknowledgements

We thank financial support by the BMBF (project: 05K2016-HEXCHEM).

References:

(1) Crabtree, G. W.; Dresselhaus; M. S.; Buchanan; M. V. The Hydrogen Economy. *Phys. Today* **2004**, *57*, 39-45.

(2) Ursua, A.; Gandia, L. M.; Sanchis, P. Hydrogen Production from Water Electrolysis: Current Status and Future Trends. *Proc. IEEE* **2012**, *100*, 410-426.

(3) Carmo, M.; Fritz, D. L.; Mergel, J.; Stolten, D. A Comprehensive Review on PEM Water Electrolysis. *Int. J. Hydrogen Energy* **2013**, *38*, 4901-4934.

(4) Trasatti, S. Electrocatalysis: Understanding the Success of DSA®. *Electrochim. Acta* **2000**, *45*, 2377-2385.

(5) Fang, Y.-H.; Liu, Z.-P. Mechanism and Tafel Lines of Electro-Oxidation of Water to Oxygen on RuO_2(110). *J. Am. Chem. Soc.* **2010**, *132*, 18214-18222.

(6) Kötz, R.; Stucki, S. Stabilization of RuO_2 by IrO_2 for Anodic Oxygen Evolution in Acid Media. *Electrochim. Acta* **1986**, *31*, 1311-1316.

(7) Cherevko, S.; Geiger, S.; Kasian, O.; Kulyk, N.; Grote, J.-P.; Savan, A.; Shrestha,, B. R.; Merzlikin, S.; Breitbach, B.; Ludwig, A.; Mayrhofer, K. J. J. Oxygen and Hydrogen Evolution Reactions on Ru, RuO_2, Ir, and IrO_2 Thin Film Electrodes in Acidic and Alkaline Electrolytes: A Comparative Study on Activity and Stability. *Catal. Today* **2016**, *262*, 170-180.

(8) Stoerzinger, K. A.; Qiao, L.; Biegalski, M. D.; Shao-Horn, Y. Orientation-Dependent Oxygen Evolution Activities of IrO_2 and RuO_2. *J. Phys. Chem. Lett.* **2014**, *5*, 1636-1641.

(9) Spöri, C.; Kwan, J. T. H.; Bonakdarpour, A.; Wilkinson, D. P.; Strasser, P. The Stability Challenges of Oxygen Evolving Catalysts: Towards a Common Fundamental Understanding and Mitigation of Catalyst Degradation. *Angew. Chem. Int. Ed.* **2017**, *56*, 5994-6021.

(10) Siracusano, S.; Hodnik, N.; Jovanovic, P.; Ruiz-Zepeda, F.; Šala, M.; Baglio, V.; Aricò, A. S. New Insights into the Stability of a High Performance Nanostructured Catalyst for Sustainable Water Electrolysis. *Nano Energy* **2017**, *40*, 618-632.

(11) Kasian, O.; Grote, J.-P.; Geiger, S.; Cherevko, S.; Mayrhofer, K. J. J. The Common Intermediates of Oxygen Evolution and Dissolution Reactions during Water Electrolysis on Iridium. *Angew. Chem. Int. Ed.* **2018**, *57*, 2488-2491.

(12) Buckley, D. N.; Burke, L. D. The Oxygen Electrode. Part 6.-Oxygen Evolution and Corrosion at Iridium Anodes. *J. Chem. Soc., Faraday Trans. 1* **1976**, *72*, 2431-2440.

(13) Hackwood, S.; Schiavone, L. M.; Dautremont-Smith; W. C.; Beni, G. Anodic Evolution of Oxygen on Sputtered Iridium Oxide Films. *J. Electrochem. Soc.* **1981**, *128*, 2569-2573.

(14) Cherevko, S.; Reier, T.; Zeradjanin, A. R.; Pawolek, Z.; Strasser, P.; Mayrhofer, K. J. J. Stability of Nanostructured Iridium Oxide Electrocatalysts during Oxygen Evolution Reaction in Acidic Environment. *Electrochem. Commun.* **2014**, *48*, 81-85.

(15) Vukovic, M. Oxygen evolution reaction on thermally treated iridium oxide films. *J. Appl. Electrochem.* **1987**, *17*, 737-745.

(16) Willinger, E.; Massué, C.; Schlögl, R.; Willinger, M. G. Identifying Key Structural Features of IrO_x Water Splitting Catalysts. *J. Am. Chem. Soc.* **2017**, *139*, 12093-12101.

(17) Danilovic, N.; Subbaraman, R.; Chang, K.-C.; Chang, S. H.; Kang, Y. J.; Snyder, J.; Paulikas, A. P.; Strmcnik, D.; Kim, Y.-T.; Myers, D.; Stamenkovic, V. R.; Markovic, N. M. Activity-Stability Trends for the Oxygen Evolution Reaction on Monometallic Oxides in Acidic Environments. *J. Phys. Chem. Lett.* **2014**, *5*, 2474-2478.

(18) Binninger, T.; Mohamed, R.; Waltar, K.; Fabbri, E.; Levecque, P.; Kötz, R.; Schmidt, T. J. Thermodynamic Explanation of the Universal Correlation between Oxygen Evolution Activity and Corrosion of Oxide Catalysts. *Sci. Rep.* **2015**, *5*, 12167.

(19) Pourbaix, M. *Atlas of Electrochemical Equilibria in Aqueous Solutions*; Pergamon Press: Oxford, U. K., 1966.

(20) Kuo, D.-Y.; Kawasaki, J. K.; Nelson, J. N.; Kloppenburg, J.; Hautier, G.; Shen, K. M.; Schlom, D. G.; Suntivich, J. Influence of Surface Adsorption on the Oxygen Evolution Reaction on IrO_2(110). *J. Am. Chem. Soc.* **2017**, *139*, 3473-3479.

(21) Kibsgaard, J.; Chorkendorff, I. Considerations for the scaling-up of water splitting catalysts. *Nature Energy* **2019**, *4*, 430-433.

(22) Novell-Leruth, G.; Carchini, G.; López, N. On the properties of binary rutile MO_2 compounds, M = Ir, Ru, Sn, and Ti: A DFT study. *J. Chem. Phys.* **2013**, *138*, 194706.

(23) Matz, O.; Calatayud, M. Periodic DFT Study of Rutile IrO_2: Surface Reactivity and Catechol Adsorption. *J. Phys. Chem. C* **2017**, *121*, 13135-13143.

(24) Lee, Y.; Suntivich, J.; May, K. J.; Perry, E. E.; Shao-Horn, Y. Synthesis and Activities of Rutile IrO_2 and RuO_2 Nanoparticles for Oxygen Evolution in Acid and Alkaline Solutions. *J. Phys. Chem. Lett.* **2012**, *3*, 399-404.

(25) Abb, M. J. S.; Herd, B.; Over, H. Template-Assisted Growth of Ultrathin Single-Crystalline IrO_2(110) Films on RuO_2(110)/Ru(0001) and Its Thermal Stability. *J. Phys. Chem. C* **2018**, *122*, 14725-14732.

(26) Herd, B.; Knapp, M.; Over, H. Atomic Scale Insights into the Initial Oxidation of Ru(0001) Using Molecular Oxygen: A Scanning Tunneling Microscopy Study. *J. Phys. Chem. C* **2012**, *116*, 24649-24660.

(27) Sohrabnejad-Eskan, I.; Goryachev, A.; Exner, K. S.; Kibler, L. A.; Hensen, E. J. M.; Hofmann, J. P.; Over, H. Temperature-Dependent Kinetic Studies of the Chlorine Evolution Reaction over RuO_2(110) Model Electrodes. *ACS Catal.* **2017**, *7*, 2403-2411.

(28) Foresti, M. L.; Pozzi, A.; Innocenti, M.; Pezzatini, G.; Loglio, F.; Salvietti, E.; Giusti, A.; D'Anca, F.; Felici, R.; Borgatti, F. In Situ Analysis Under Controlled Potential Conditions: An Innovative Setup and Its Application to the Investigation of Ultrathin Films Electrodeposited on Ag(111). *Electrochim. Acta* **2006**, *51*, 5532-5539.

(29) Weber, T.; Abb, M. J. S.; Khalid, O.; Pfrommer, J.; Carla, F.; Znaiguia, R.; Vonk, V.; Stierle, A.; Over, H. In Situ Studies of the Electrochemical Reduction of a Supported Ultrathin Single-Crystalline RuO_2(110) Layer in an Acidic Environment. *J. Phys. Chem. C* **2019**, *123*, 3979-3987.

(30) He, Y. B.; Knapp, M.; Lundgren, E.; Over, H. Ru(0001) Model Catalyst under Oxidizing and Reducing Conditions: In-Situ High-Pressure Surface X-ray Diffraction Study. *J. Phys. Chem. B* **2005**, *109*, 21825-21830.

(31) Kim, Y. D.; Seitsonen, A. P.; Over, H. The Atomic Geometry of Oxygen-Rich Ru(0001) Surfaces: Coexistence of (1×1)O and RuO_2(110) Domains. *Surf. Sci.* **2000**, *465*, 1-8.

(32) Björck, M.; Andersson, G. GenX: An Extensible X-Ray Reflectivity Refinement Program Utilizing Differential Evolution. *J. Appl. Cryst.* **2007**, *40*, 1174-1178.

(33) Rolison, D. R.; Long, J. W.; Lytle, J. C.; Fischer, A. E.; Rhodes, C. P.; McEvoy, T. M.; Bourg, M. E.; Lubers, A. M. Multifunctional 3D nanoarchitectures for energy storage and conversion. *Chem. Soc. Rev.* **2009**, *38*, 226-252.

(34) Krause, P. P. T.; Camuka, H.; Leichtweiss, T.; Over, H. Temperature-Induced Transformation of Electrochemically Formed Hydrous RuO_2 Layers over Ru(0001) Model Electrodes. *Nanoscale* **2016**, *8*, 13944-13953.

(35) Hepel, T.; Pollak, F. H.; O'Grady, W. E. Irreversible Voltammetric Behavior of the (100) IrO_2 Single-Crystal Electrodes in Sulfuric Acid Medium. *J. Electrochem. Soc.* **1985**, *132*, 2385-2390.

(36) Kim, S. H.; Wintterlin, J. Morphology of RuO_2(110) Oxide Films on Ru(0001) Studied by Scanning Tunneling Microscopy. *J. Chem. Phys.* **2009**, *131*, 064705.

(37) Chen, R.; Trieu, V.; Zeradjanin, A. R.; Natter, H.; Teschner, D.; Kintrup, J.; Bulan, A.; Schuhmann, W.; Hempelmann, R. Microstructural Impact of Anodic Coatings on the Electrochemical Chlorine Evolution Reaction. *Phys. Chem. Chem. Phys.* **2012**, *14*, 7392-7399.

(38) Scott, S. L. A Matter of Life(time) and Death. *ACS Catal.* **2018**, *8*, 8597-8599.

For Table of Contents Only